

## Full paper

Efficiency enhancement of InGaN/GaN blue light-emitting diodes with top surface deposition of AlN/Al<sub>2</sub>O<sub>3</sub>Kwangeun Kim<sup>a</sup>, Mengyuan Hua<sup>b,1</sup>, Dong Liu<sup>a,1</sup>, Jisoo Kim<sup>a</sup>, Kevin J. Chen<sup>b,\*</sup>, Zhenqiang Ma<sup>a,\*</sup><sup>a</sup> Department of Electrical and Computer Engineering, University of Wisconsin-Madison, Madison, WI 53706, United States<sup>b</sup> Department of Electronic and Computer Engineering, Hong Kong University of Science and Technology, Clear Water Bay, Hong Kong, China

## ARTICLE INFO

## Keywords:

Efficiency droop  
Light-emitting diodes  
AlN  
GaN  
Carrier injection  
Quantum-confined Stark effect

## ABSTRACT

Improving the energy conversion efficiency of light-emitting diodes (LEDs) for blue light emission has been a continuing pursuit for the past several decades. Here, we report InGaN/GaN LEDs with improved energy efficiency through the simple deposition of multifunctional ultrathin AlN/Al<sub>2</sub>O<sub>3</sub> layers on top of p-type GaN (i.e., GaN:Mg) using remote plasma pretreatment and plasma-enhanced atomic-layer deposition (PEALD). The AlN/Al<sub>2</sub>O<sub>3</sub> stacked layers played principal roles in improving the LED energy efficiency: 1) The surface defect states of p-type GaN were reduced to minimize leakage current and oxidation was prevented by passivating the GaN surface; 2) the net positive charges formed at the AlN/GaN interface enhanced the hole injection rate into the multi-quantum well (MQW) by formation of downward band bending with the increased surface potential; and 3) the increased hole injection rate induced the band-filling effect and screening of internal polarization fields in the MQW. The AlN/Al<sub>2</sub>O<sub>3</sub> stacked layers deposited on the GaN:Mg have overall improved the radiative recombination rate of the InGaN/GaN LEDs and thus light-emission efficiency. X-ray photoelectron spectroscopy was used to characterize the surface potential change of GaN. The peak efficiency values of wall-plug efficiency, the external-quantum efficiency, and the efficacy of the AlN/Al<sub>2</sub>O<sub>3</sub> coated InGaN/GaN LEDs were improved by 29%, 29%, and 30%, respectively. The corresponding efficiency droop rates were decreased by 13%, 6% and 3%, respectively, as compared to those of reference LEDs.

## 1. Introduction

Over the past decades, improving energy conversion efficiency of InGaN/GaN blue light-emitting diodes (LEDs) has been persistently pursued since its first invention in 1993 [1]. The continuous improvement of energy efficiency of the InGaN/GaN LEDs mainly originated from developments in wafer growth techniques, packaging technologies, and nanophotonics [2–15]. The major bottleneck toward achieving high efficiency LEDs is the low hole injection rate from the p-type hole transport layer (p-GaN:Mg) due to insufficient activation of the p-type dopant. The poor hole injector leads to significant imbalance of the number of electrons and holes, thus low efficiency at high current densities [16–19]. A number of research efforts have been geared toward making a breakthrough in this issue, including formation of a surface polarization layer, electron blocking layer, tunnelling layer, graded barrier structure, and nanopatterning [17,20–23]. While these approaches helped improve energy conversion efficiency, there still exist issues such as high cost for wafer regrowth and nonuniformity for surface patterning over a full-wafer area, in addition to strain induced

by different coefficients of thermal expansion and different lattice constants between substrates and epitaxial layers.

The InGaN/GaN LEDs grown on a c-plane sapphire substrate possess a piezo-electric polarization field induced by the lattice mismatch between active InGaN and underlying GaN layers. Additionally, the Wurtzite crystal structure of GaN generates a spontaneous polarization field in the LEDs, which consequently forms tiled energy bands within the InGaN/GaN multi-quantum wells (MQWs), leading to reduced spatial distribution of electron and hole wave functions and thus reduced radiative recombination rates (i.e., quantum-confined Stark effect (QCSE)) [24–29]. Several methods were attempted to suppress the QCSE in LEDs, such as adaptation of nonpolar or semipolar substrates, polar MQWs with large wave function overlap design, substrate variation, polarization-matched epi-layer, top surface modification, and 1-dimensional vertical structure array [2,4,5,14,15,28–35]. These methods require complicated device design, special/expensive substrates, and skillful epitaxy techniques. Various processes for LED top surface modification were also attempted including surface texturing, less-strained layer growth, and thin layer deposition [28,30,34,35].

\* Corresponding authors.

E-mail addresses: [eejkchen@ust.hk](mailto:eejkchen@ust.hk) (K.J. Chen), [mazq@engr.wisc.edu](mailto:mazq@engr.wisc.edu) (Z. Ma).<sup>1</sup> These authors contributed equally.

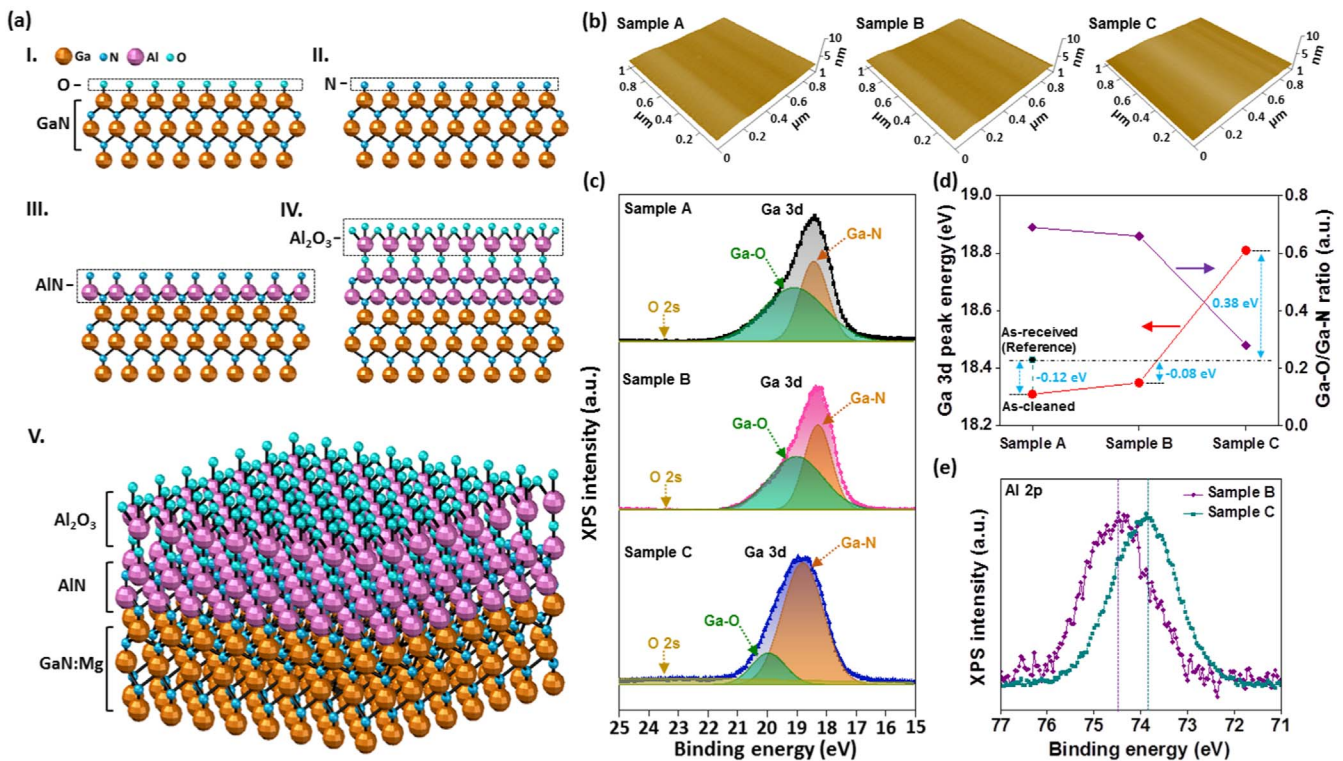


**Fig. 1.** Surface structure and properties of AlN/Al<sub>2</sub>O<sub>3</sub>-coated GaN:Mg layer on top of InGaN/GaN LEDs. (a) Formation of AlN/Al<sub>2</sub>O<sub>3</sub> stacked layer on the GaN:Mg through remote plasma pretreatment (RPP) and plasma-enhanced atomic layer deposition (PEALD). I. As-received GaN LED epi-wafer with surface oxide layer. II. *In situ* RPP native oxide removal and nitridation. III. PEALD AlN monolayer deposition. IV. PEALD Al<sub>2</sub>O<sub>3</sub> deposition. V. Atomic crystal structure of the GaN:Mg with top surface deposition of AlN/Al<sub>2</sub>O<sub>3</sub> stacked layer. (b) Surface roughness of the three types of samples characterized by AFM. The root-mean square ( $R_{rms}$ ) values for reference GaN LED wafer (sample A), Al<sub>2</sub>O<sub>3</sub>-coated GaN LED wafer (sample B), and AlN/Al<sub>2</sub>O<sub>3</sub>-coated GaN LED wafer (sample C) are 1.32 nm, 1.30 nm, and 1.24 nm, respectively. (c) X-ray photoelectron spectroscopy (XPS) of Ga 3d core level spectra for the three samples. Ga-N and Ga-O denote Ga bonded to N and Ga bonded to O, respectively. (d) Plot of Ga 3d peak binding energy and Ga-O/Ga-N intensity ratio for the three samples. The Ga 3d binding energies of as-received and as-cleaned sample A are indicated separately. (e) XPS Al 2p binding energy comparison between samples B and C.

Although these surface modification approaches are simpler than other epitaxial methods, the cost associated with these approaches may still be high.

AlN was proved to be an efficient III–nitride passivation material for GaN-based devices with low interface states [36–41]. However, the AlN can be easily oxidized in air and the oxidation of AlN completely degrades the material properties. Al<sub>2</sub>O<sub>3</sub> is also a passivation material but not a polarized material. By coating a conventional Al<sub>2</sub>O<sub>3</sub> on top of AlN to form stacked AlN/Al<sub>2</sub>O<sub>3</sub> layers on top of GaN, the AlN then acts as an interface blocking layer that prevents Ga-O formation between Al<sub>2</sub>O<sub>3</sub> and GaN, while maintaining its polarization properties. As a result, the stacked AlN/Al<sub>2</sub>O<sub>3</sub> layers can significantly improve the passivation quality in terms of surface states of leakage as compared to that of Al<sub>2</sub>O<sub>3</sub> passivation. Previously, the polarization charges of AlN deposited by atomic layer deposition (ALD) were successfully used to compensate the slow-response surface states in AlGaIn/GaN high-electron-mobility transistors and thus to prevent the 2-D electron gas channel from being pinched off [39]. Up to now, no investigations on the influences of AlN/Al<sub>2</sub>O<sub>3</sub> polarization layers on the performance of InGaN/GaN LEDs were found in existing literature.

In this paper, we report the detailed studies on the impact of plasma-enhanced ALD (PEALD) AlN/Al<sub>2</sub>O<sub>3</sub> on the energy conversion efficiency of InGaN/GaN blue LEDs. We used X-ray photoelectron spectroscopy (XPS) to characterize the surface potential changes inside the p-GaN layer of InGaN/GaN LEDs coated with AlN/Al<sub>2</sub>O<sub>3</sub> stacked layers. We discovered three roles of PEALD AlN/Al<sub>2</sub>O<sub>3</sub> on the InGaN/GaN LEDs. 1) The surface defect states of p-GaN in relation to leakage and oxidation were reduced by the passivation function of the layers. 2) The hole injection rate into the MQW was enhanced by the increased surface potential of p-GaN. The surface recombination of holes on the p-GaN was also reduced by the increased surface potential. 3) The QCSE

in the MQW was suppressed by the band-filling effect and screening of the internal polarization fields with the increased hole injection. As a result of the above factors, the radiative recombination rate and light emission efficiency of the InGaN/GaN LEDs were improved with reduced efficiency droop rates.

## 2. Experimental section

### 2.1. InGaN/GaN LED wafer preparation

The InGaN/GaN LED wafers were grown on patterned sapphire substrate (PSS) along the (0001)-orientation by metal organic chemical vapor deposition (MOCVD). An undoped GaN buffer layer was grown first, followed by a 600 nm Si-doped GaN layer with a doping concentration of  $\sim 10^{19} \text{ cm}^{-3}$  and a  $\sim 350 \text{ nm}$  GaN grading layer. Next, an eight-period InGaN/GaN MQW with a targeted wavelength of  $\sim 450 \text{ nm}$  was grown. The growth of the LED structure was finished with a Mg-doped GaN layer. After epi-growth, the LED wafers were subject to sonication in acetone/isopropyl alcohol at room temperature (RT) (Note: at this state the sample is labelled as “as-received”), followed by RCA cleaning to remove organic and ionic debris and surface oxide (Note: the state of the sample is now labelled as “as-cleaned”. If the “as-cleaned” sample is exposed to ambient for long, it returns to “as-received” state). Three samples were prepared in the experiment. The reference sample A in the following context is a bare InGaN/GaN LED wafer with no deposition of oxide (“as-received” state). Samples B and C are the InGaN/GaN LED wafers coated with 1 nm Al<sub>2</sub>O<sub>3</sub> using conventional ALD and 0.6 nm/1.0 nm AlN/Al<sub>2</sub>O<sub>3</sub> using PEALD on sample A, respectively.

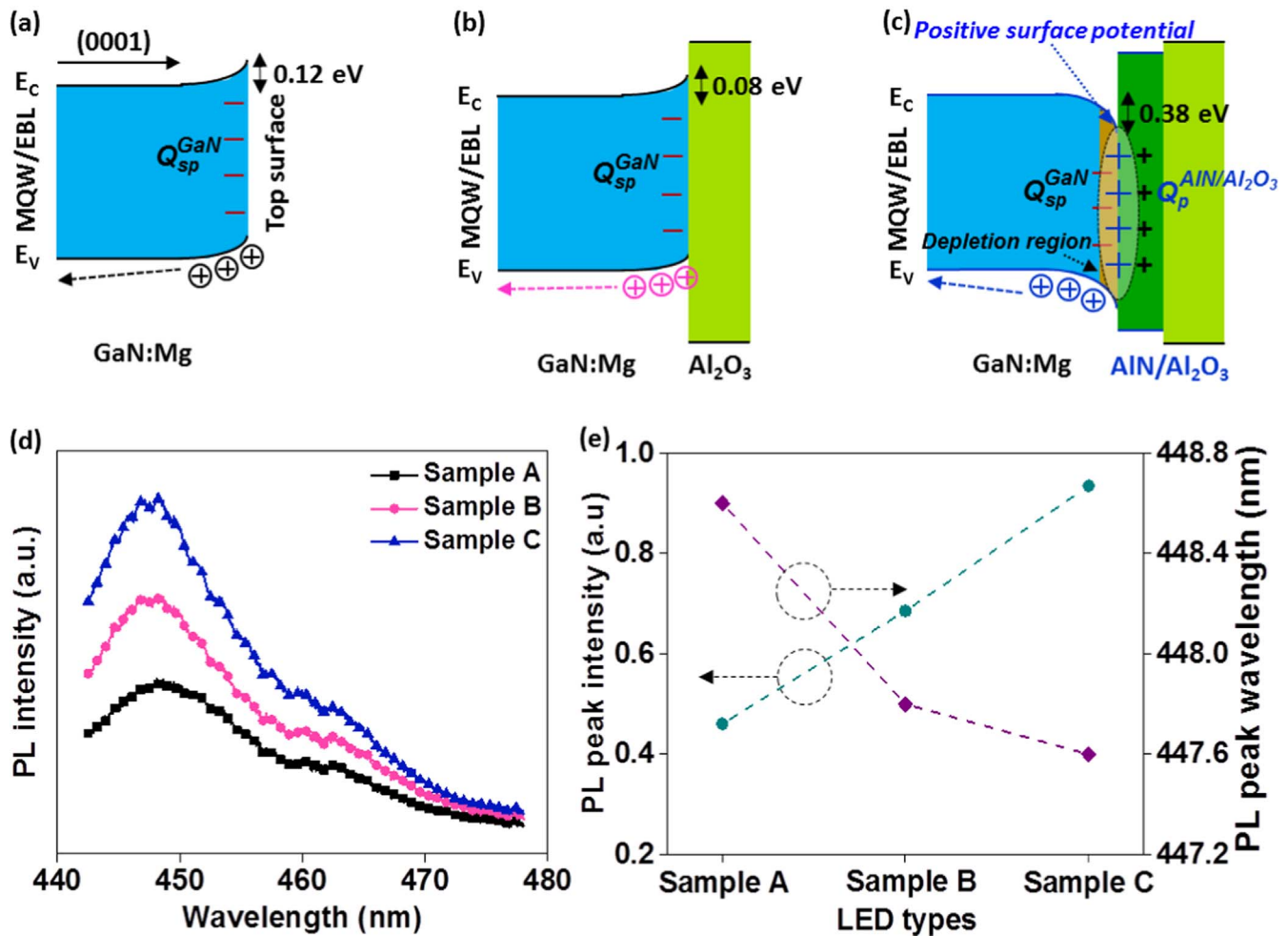


Fig. 2. Surface potential and band bending. The band bending illustrations for (a) sample A (as-cleaned) (b) sample B, and (c) sample C.  $Q_{sp}^{GaN}$  and  $Q_{sp}^{AlN/Al_2O_3}$  indicate the polarization charges in the top p-GaN and AlN/Al<sub>2</sub>O<sub>3</sub> layers, respectively. In the case of downward band bending (c), hole injection rate into multi-quantum well (MQW) is increased due to higher potential energy. + and – denote the positive and negative polarization charges. (d) Photoluminescence (PL) spectra of the three samples. (e) Plot of the PL peak intensity and wavelength of the three samples.

## 2.2. PEALD process

After a wet cleaning procedure, the LED wafer (for sample C) was loaded into the PEALD system. An in situ remote plasma pretreatment (RPP) process in sequence with NH<sub>3</sub>-Ar-N<sub>2</sub> plasma was performed to remove surface native oxides on GaN. After the RPP process, the 0.6 nm AlN monolayer using N<sub>2</sub>-H<sub>2</sub> and trimethylaluminum (TMA) precursors and the 1 nm Al<sub>2</sub>O<sub>3</sub> layer using H<sub>2</sub>O and TMA precursors were chronologically deposited by PEALD with a growth rate of 0.6 Å/cycle. The RPP and PEALD were carried out at a substrate temperature of 300 °C. The detailed process is described elsewhere previously [36,41]. The thicknesses of the AlN/Al<sub>2</sub>O<sub>3</sub> stacked layers were measured by an ellipsometer.

## 2.3. XPS measurements

The elements' core energy level shifts in the top Mg-doped GaN layers of the reference (no coating, sample A), Al<sub>2</sub>O<sub>3</sub>-coated (sample B), and AlN/Al<sub>2</sub>O<sub>3</sub>-coated (sample C) GaN LED wafers were measured using XPS. The valence band maximum (VBM) and core levels of Ga 3d, Al 2p, C 1s, N 1s, and O 1s were scanned to analyse the surface potential changes of the GaN under different oxide coating conditions. A monochromatic Al Kα ( $h\nu = 1486.60$  eV) X-ray source with a 90° take-off angle (normal to surface) was used with filament current of 1.66 A, emission current of 2.98 mA, and accelerating voltage of 12 kV. The

scans were repeated 20 times with a survey step of 0.01 eV, spot size of 100 μm, pass energy of 50 eV, and dwell time of 50 ms. The XPS equipment was calibrated using the standard peak positions at 933.00 eV of Cu 2p<sub>3/2</sub>, 368.20 eV of Ag 3d<sub>5/2</sub>, and 84.00 eV of Au 4f<sub>7/2</sub>. The 284.80 eV of C 1s peak was referenced to offset the binding energy shift induced by surface peak charge. The uncertainty of core level centers is ± 0.015 eV.

## 2.4. Fabrication of GaN LEDs

GaN LEDs were fabricated on the XPS-characterized reference, Al<sub>2</sub>O<sub>3</sub>-, and AlN/Al<sub>2</sub>O<sub>3</sub>-GaN LED wafers, respectively. The three types of LEDs were fabricated together from the beginning to the end of the process. Ni/Au (5/300 nm) was deposited for anodes, followed by cathode mesa etching using inductively coupled plasma with BCl<sub>3</sub>, Cl<sub>2</sub>, and Ar gas at a flow rate of 10, 16, and 3 sccm, respectively, 100/500 W ICP/RF power, 190 V DC voltage, and 4 mT pressure. Ti/Al (5/300 nm) was deposited for cathodes and a subsequent ohmic annealing was carried out at 500 °C for 30 s in N<sub>2</sub> ambient for both anodes and cathodes. All electrodes were formed by photolithography, e-beam evaporation, and lift-off. After isolation, the active area of GaN LEDs was defined to be 0.0025 cm<sup>2</sup>. The fabricated GaN LEDs were aluminium wire-bonded for efficiency measurements using an integration sphere. No light extraction fixtures were used for three types of fabricated LEDs.

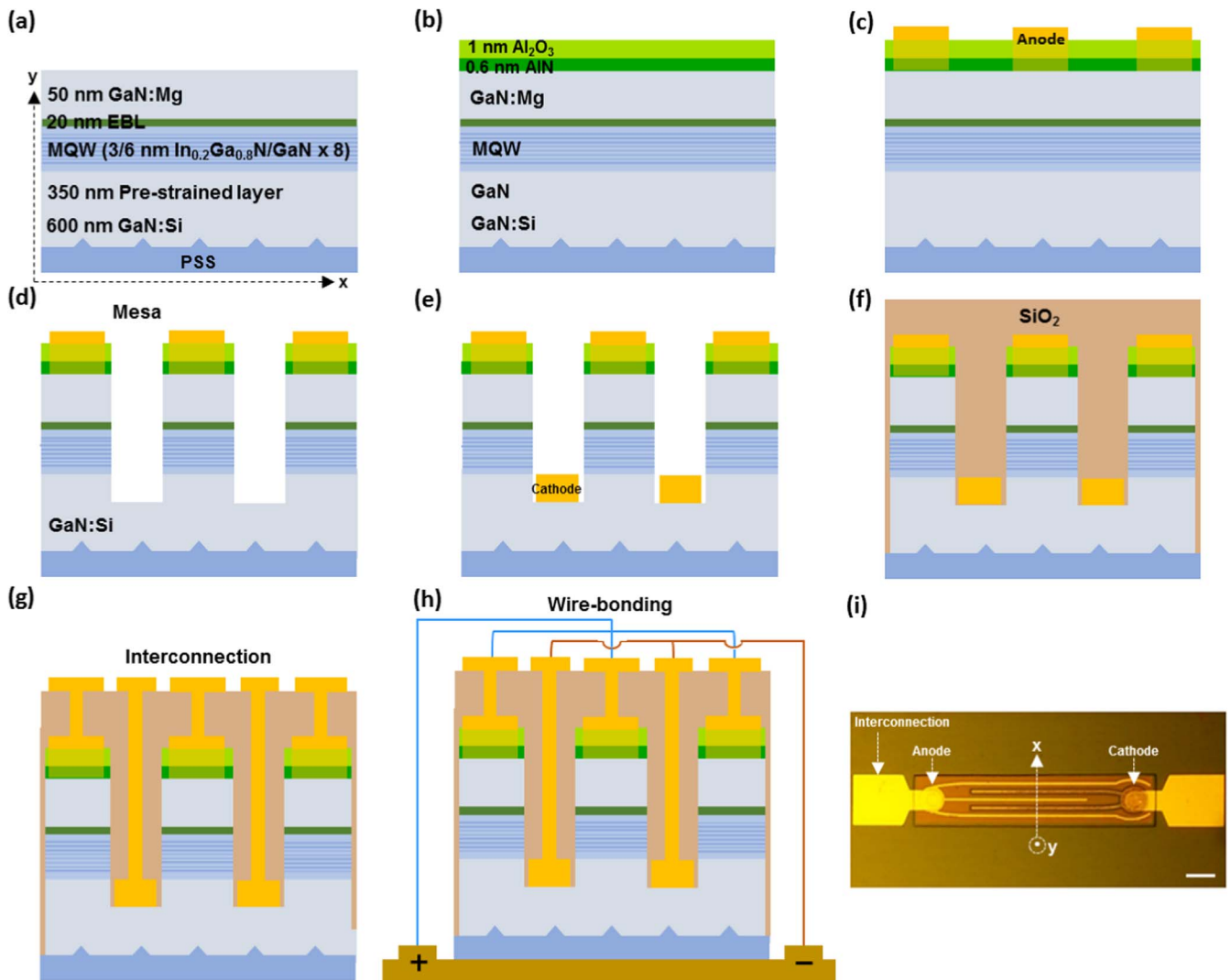


**Fig. 3.** Process steps for AlN/Al<sub>2</sub>O<sub>3</sub>-GaN LEDs. (a) GaN LED epi-wafer cleaning and remote plasma pretreatment (RPP) process. (b) Plasma-enhanced atomic-layer deposition (PEALD) of AlN/Al<sub>2</sub>O<sub>3</sub>. (c) Deposition of anode electrodes and ohmic annealing. (d) Cathode mesa etching. (e) Deposition of cathode electrodes and ohmic annealing. (f) Plasma-enhanced chemical vapor deposition (PECVD) of SiO<sub>2</sub>. (g) Via hole etching and interconnection metal deposition. (h) Wire-bonding for measurement. (i) Optical image of the fabricated AlN/Al<sub>2</sub>O<sub>3</sub>-GaN LEDs, scale bar = 100 μm.

## 2.5. Characterizations

The morphologies of the three types of LED wafers were characterized by a Bruker Multimode 8 atomic force microscopy (AFM). I-V characteristics were measured using a Keithley 4200-SCS semiconductor characterization system. Photoluminescence (PL) spectra were obtained using a Horiba Jobin Yvon Labram Aramis Raman spectrometer equipped with a He-Cd laser source. Electroluminescence (EL) spectra were acquired using a Gamma Scientific GS-1290 spectroradiometer with a calibrated integration sphere. Input bias for efficiency measurements was supplied by a Keithley 2602B system source meter. Chemical bonding states were analysed by a Thermo Scientific K-Alpha + XPS. All measurements were made at RT.

## 3. Results and discussion

### 3.1. Surface characterizations

Fig. 1a illustrates the formation of top surface AlN/Al<sub>2</sub>O<sub>3</sub> stacked layers on the GaN:Mg layer of InGaN/GaN LED wafer through the RPP and PEALD processes (sample C). It begins with LED wafer preparation (I), followed by RPP native oxide removal and surface nitridation (II),

PEALD of 0.6 nm AlN monolayer (III), and PEALD of 1 nm Al<sub>2</sub>O<sub>3</sub> stack layer (IV). The deposition of the AlN interface layer was precisely controlled to be one monolayer [40]. An atomic crystal structure of sample C after finishing the PEALD exhibits the AlN/Al<sub>2</sub>O<sub>3</sub> stacked layers deposited on the GaN:Mg (V). The crystalline property of the PEALD AlN monolayer between GaN and Al<sub>2</sub>O<sub>3</sub> was examined using transmission electron microscopy (TEM) in our previous studies, in which the Wurtzite GaN, monocrystal-like AlN, and amorphous Al<sub>2</sub>O<sub>3</sub> properties were characterized (Fig. S2) [38,41]. The AFM scans as shown in Fig. 1b exhibit the surface roughness of the samples, in which the root-mean square ( $R_{rms}$ ) values for samples A, B, and C were 1.32 nm, 1.30 nm, and 1.24 nm, respectively.

The passivation properties of the AlN/Al<sub>2</sub>O<sub>3</sub> layers for the GaN:Mg were analysed by XPS measurements. AlN/Al<sub>2</sub>O<sub>3</sub> with a total thickness of 1.6 nm is suitable for XPS characterizations since photoelectrons can escape 10 nm deep from the surface. The XPS Ga 3d core levels of the three samples (before LED fabrication) were obtained and divided into three components: Ga bonded to N (Ga-N), Ga bonded to O (Ga-O), and O 2s peaks as shown in Fig. 1c. For samples A, B and C, the Ga 3d binding energies were 18.43, 18.35, and 18.81 eV, respectively, and the peak intensity ratios of Ga-O/Ga-N were 0.69, 0.66, and 0.28, respectively, as shown in Fig. 1d. The Ga 3d binding energy of as-cleaned

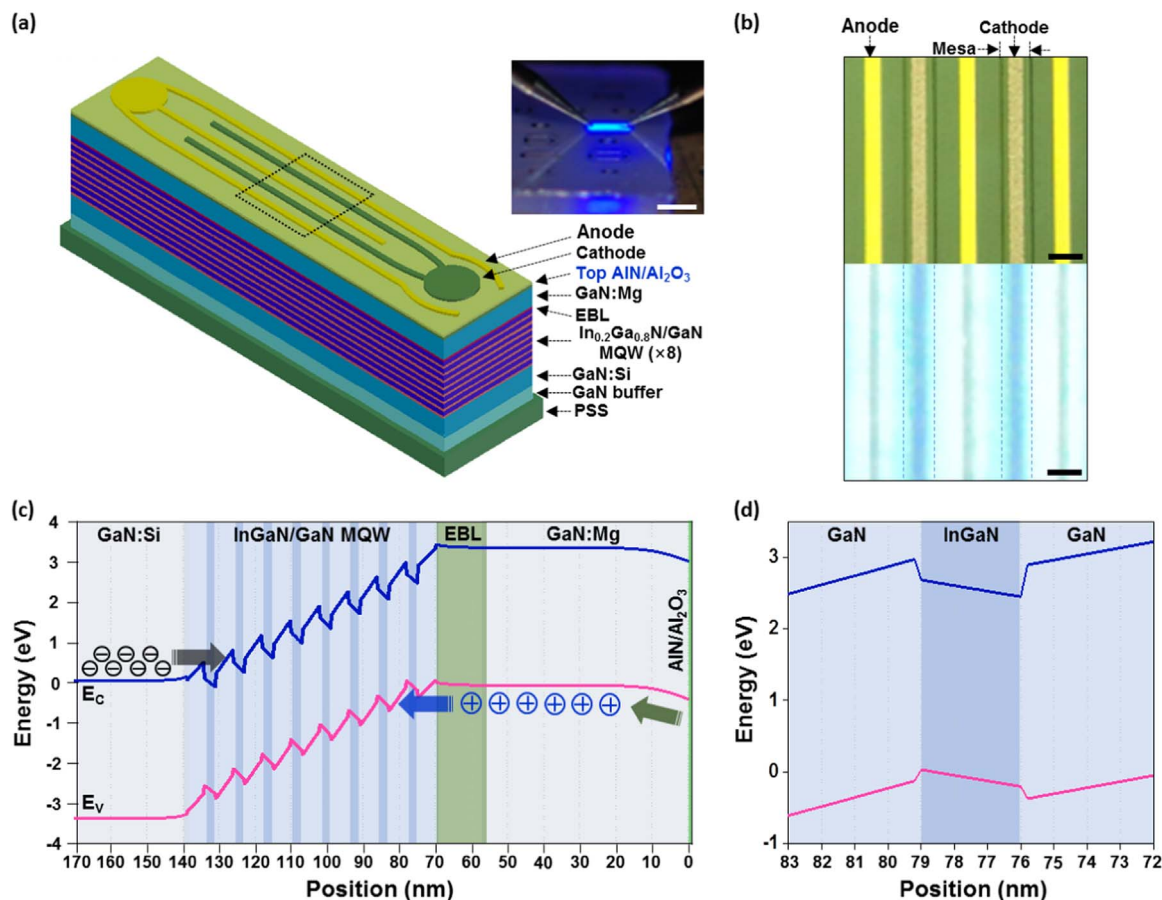


Fig. 4. Structure of AlN/Al<sub>2</sub>O<sub>3</sub>-GaN LEDs. (a) The vertical structure of GaN LEDs with top surface AlN/Al<sub>2</sub>O<sub>3</sub> layer. Inset shows light emission from sample C LED, scale bar = 1 mm. (b) Optical image of anode and cathode electrodes (top) and light-emission from the electrodes at current density 10 A/cm<sup>2</sup> (bottom), scale bar = 20 μm. No current crowding effect was observed. (c) Calculated energy band diagram of the LEDs with the AlN/Al<sub>2</sub>O<sub>3</sub> layer. (d) Energy band diagram of a single QW nearby the EBL/GaN:Mg layers.

sample A (18.31 eV) was added in Fig. 1d for an estimation of band bending (as plotted in Fig. 2a). The Ga 3d binding energy of the GaN decreased with Al<sub>2</sub>O<sub>3</sub> deposition (sample B) and increased with AlN/Al<sub>2</sub>O<sub>3</sub> deposition (sample C), compared to that of the reference GaN LED wafer (sample A). The increased Ga 3d binding energy with the AlN/Al<sub>2</sub>O<sub>3</sub> stacked layers indicated the increased surface potential of GaN. The decreased Ga-O/Ga-N ratio with the Al<sub>2</sub>O<sub>3</sub> layer and the further decreased ratio with the AlN/Al<sub>2</sub>O<sub>3</sub> stacked layers proved the better passivation quality of AlN/Al<sub>2</sub>O<sub>3</sub> in relation to Al<sub>2</sub>O<sub>3</sub>. Since the enthalpy for the formation of Ga-O and Ga-N bonds are -545 kJ/mol and -110 kJ/mol, individually, the Ga-O bond is more stable than the Ga-N bond; thus, the oxygen atoms can easily incorporate into GaN surface under ambient air or during Al<sub>2</sub>O<sub>3</sub> deposition [42]. The ratio of Ga-O/Ga-N of sample A represents the natural surface oxidation ratio of GaN. For sample B, the ratio represents a measure of oxidation of the GaN surface during ALD Al<sub>2</sub>O<sub>3</sub>. Due to the TMA precursor pulse at the beginning of the ALD process, the surface oxide of GaN (Ga-O bond) was removed first by “clean up effect” and the Al<sub>2</sub>O<sub>3</sub> film was deposited on the GaN [43]. Thus, the ratio of Ga-O/Ga-N of sample B indicates the oxidation ratio of GaN from the ALD process, in which the GaN surface absorbed the oxygen atoms from the Al<sub>2</sub>O<sub>3</sub> film. In the case of sample C, however, the ratio of Ga-O/Ga-N was much decreased in comparison to samples A and B. This is due to RPP removal of the surface oxide of GaN prior to the ALD process and the subsequent PEALD AlN which completely prevents the GaN surface from oxidation with oxygen atoms of the Al<sub>2</sub>O<sub>3</sub> film on AlN. The detectable O 2s peak on sample C is due to the unabsorbed oxygen atoms, in contrast to samples A and B in which the oxygen atoms contribute to the formation of Ga-O bonds. The TEM image demonstrates no interface/surface oxidation on GaN during AlN/

Al<sub>2</sub>O<sub>3</sub> deposition (Fig. S1). Therefore, the Ga 3d peak of sample C was obtained from the oxidation-free GaN surface. The shift in Ga 3d binding energy and corresponding surface potential of sample C are attributed solely to the AlN/Al<sub>2</sub>O<sub>3</sub> top surface deposition. Regarding the ratio of Ga-O/Ga-N of sample C, it might be related to the maximum atomic percentage of oxygen (25%) the GaN lattice can accommodate inside with no change in the Wurtzite crystal structure [42,44]. Fig. 1e shows the XPS Al 2p core level binding energies of samples B and C, which were 74.48 and 73.89 eV, respectively. The shift of the Al 2p core level binding energy is due to the different band gaps of two interface materials (i.e., AlN versus Al<sub>2</sub>O<sub>3</sub>).

### 3.2. Surface band characteristics

The shifts in the binding energy of the atomic core levels due to the different interface/surface conditions induce surface potential changes and the corresponding band bending situations. Based on the XPS results (Fig. 1c and d), the band bending and surface potential of the three types of LEDs are depicted in Fig. 2a-c, respectively. The Ga 3d binding energy of as-received sample A (Fig. 1d) is referenced to estimate the band bending. It is noted that sample A under as-cleaned state shows upward band bending with 0.12 eV surface potential in comparison to that under as-received state (Fig. 2a. and Fig. S2). The upward band bending of sample A was originated from the negative bound sheet charges that come from the internal spontaneous polarization field in the GaN (Fig. 2a) [45]. Due to the upward valence band bending, holes in the GaN are “confined” in the potential valley, which impedes hole injection. The deposition of the Al<sub>2</sub>O<sub>3</sub> layer (sample B) resulted in a lower surface potential and band bending as compared to that of sample

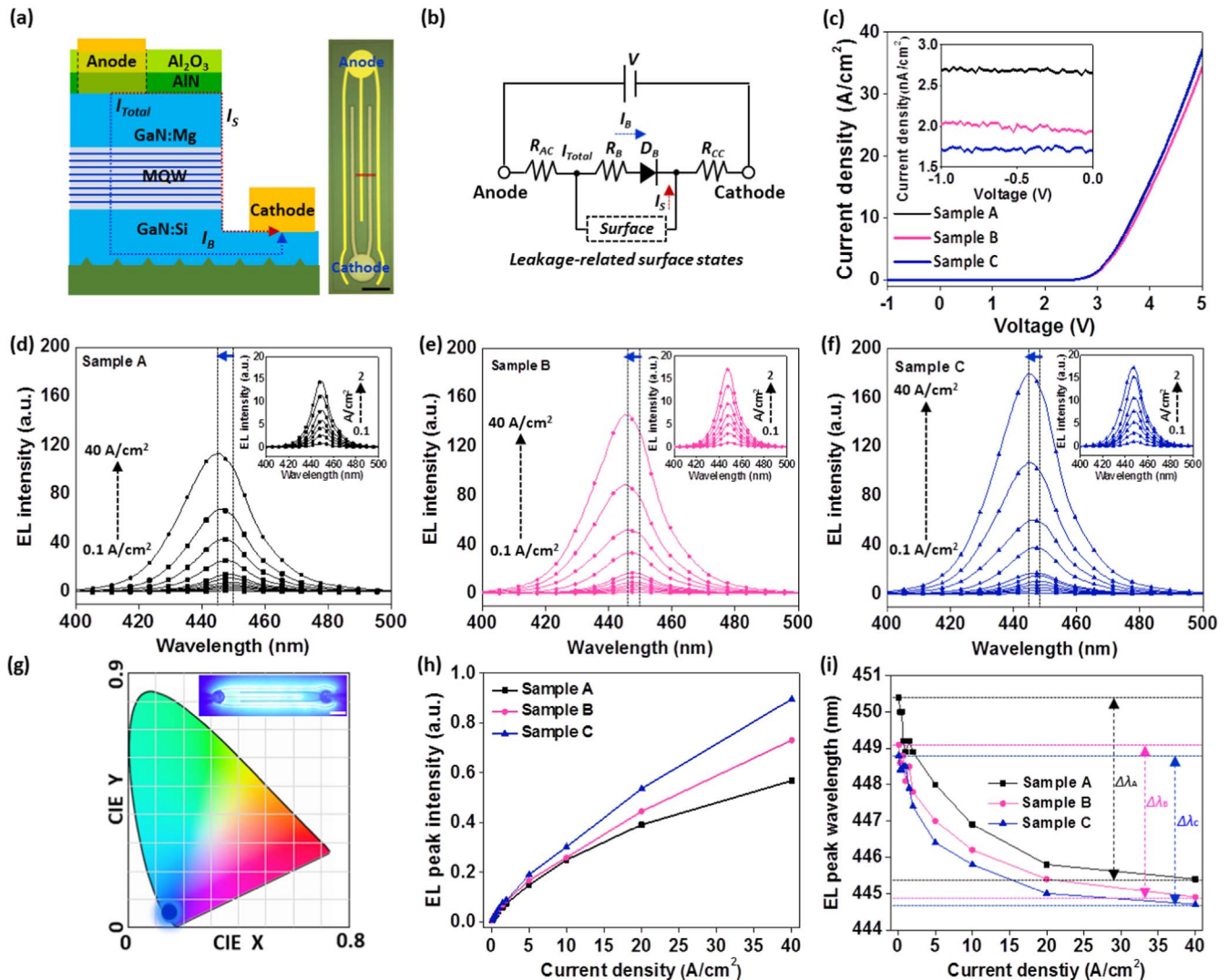


**Fig. 5.** Electrical characteristics of the LEDs. (a) Vertical structure of AlN/Al<sub>2</sub>O<sub>3</sub>-GaN LEDs. The  $I_{Total}$  is divided into the bulk current ( $I_B$ ) and the shunt current ( $I_S$ ). Inset shows an optical image of the top view of a fabricated LED, scale bar = 100  $\mu$ m. The red solid line indicates the horizontal region for the vertical structure. (b) Equivalent circuit of the LEDs.  $R_{AC}$  and  $R_{CC}$  are anode and cathode contact resistances, respectively.  $R_B$  is bulk series resistance and  $D_B$  the ideal bulk p-n diode.  $R_C$ ,  $R_B$ , and  $D_B$  are fixed.  $I_S$  varies according to the condition of surface states. (c) Current density-voltage ( $J$ - $V$ ) characteristics of the LEDs. The inset shows the leakage current characteristics of the three types LEDs under reverse bias. Electroluminescence (EL) spectra of (d) sample A, (e) sample B, and (f) sample C at driving current densities of 0.1, 0.3, 0.5, 0.7, 1, 1.5, 2, 5, 10, 20, and 40 A/cm<sup>2</sup>. The dashed lines in (d), (e), and (f) indicate the peak wavelength at 0.1 and 40 A/cm<sup>2</sup>. Insets in d-f represent the EL spectra at low current densities of 0.1, 0.3, 0.5, 0.7, 1, 1.5, and 2 A/cm<sup>2</sup>. (g) The CIE1931 chromaticity diagram including the chromaticity coordinates of EL spectra from the LEDs. Inset shows the light-emission image of sample C LED captured at 10 A/cm<sup>2</sup>, scale bar = 100  $\mu$ m. (h) Plot of the EL peak intensity as a function of current density of the LEDs. The increased EL peak intensities of samples B and C are ascribed to the increased electron-hole recombination rate by the surface passivation and enhanced hole injection rate. (i) Plot of the EL peak wavelength as function of current density for the three types LEDs, indicating the blue shift of sample A ( $\Delta\lambda_A$ ), sample B ( $\Delta\lambda_B$ ), and sample C ( $\Delta\lambda_C$ ).

A, which exhibits a surface potential of only 0.08 eV but still with upward bending (Fig. 2b). For sample C, a 0.38 eV surface potential and downward band bending were formed on the surface of the GaN:Mg (Fig. 2c). The change in the band bending direction from upward bending in sample A and B to downward bending in sample C indicates that positive surface charges were formed at the GaN/AlN interface, which is solely due to the deposition of the AlN/Al<sub>2</sub>O<sub>3</sub> layers. From the capacitance-voltage measurements in our previous study, a fixed sheet positive charge density of  $\sim 3.20 \times 10^{13}$  cm<sup>-2</sup> was formed [39]. Due to the monocrystal-like structure of the PEALD-AlN layer (Fig. S1), the positive charges can be considered polarization charges. The positive surface charges at the interface induced by the AlN/Al<sub>2</sub>O<sub>3</sub> have overcompensated for the negative spontaneous polarization charges of  $2.10 \times 10^{13}$  cm<sup>-2</sup> in the GaN. Therefore, positive surface potential of GaN at the interface was formed, which leads to downward band bending at the surface of GaN and facilitates hole injection into the MQW [45]. The combination of the above situations lead to a reduced surface

recombination of holes.

Fig. 2d shows the PL spectra of the three samples. The peak wavelengths of samples A, B and C LEDs are 448.6 nm, 447.8 nm, and 447.6 nm, respectively, with gradual increasing peak intensities (Fig. 2e) that were measured under the same conditions. The increased PL intensities of samples B and C, compared to sample A, are attributed to the reduced surface recombination of holes. The blue shift in the peak wavelengths is possibly due to the reduced internal polarization field in the GaN that was caused by the compensation of surface polarization charges due to top layer depositions [28].

### 3.3. LED process and structures

The structure of the LEDs with the top surface layer is described in Fig. 3, in which the GaN LED epi-wafer was first deposited with the AlN/Al<sub>2</sub>O<sub>3</sub> layer (Fig. 3b) and the anode electrodes were formed on the top surface of the AlN/Al<sub>2</sub>O<sub>3</sub>-deposited GaN epi-wafer (Fig. 3c). The

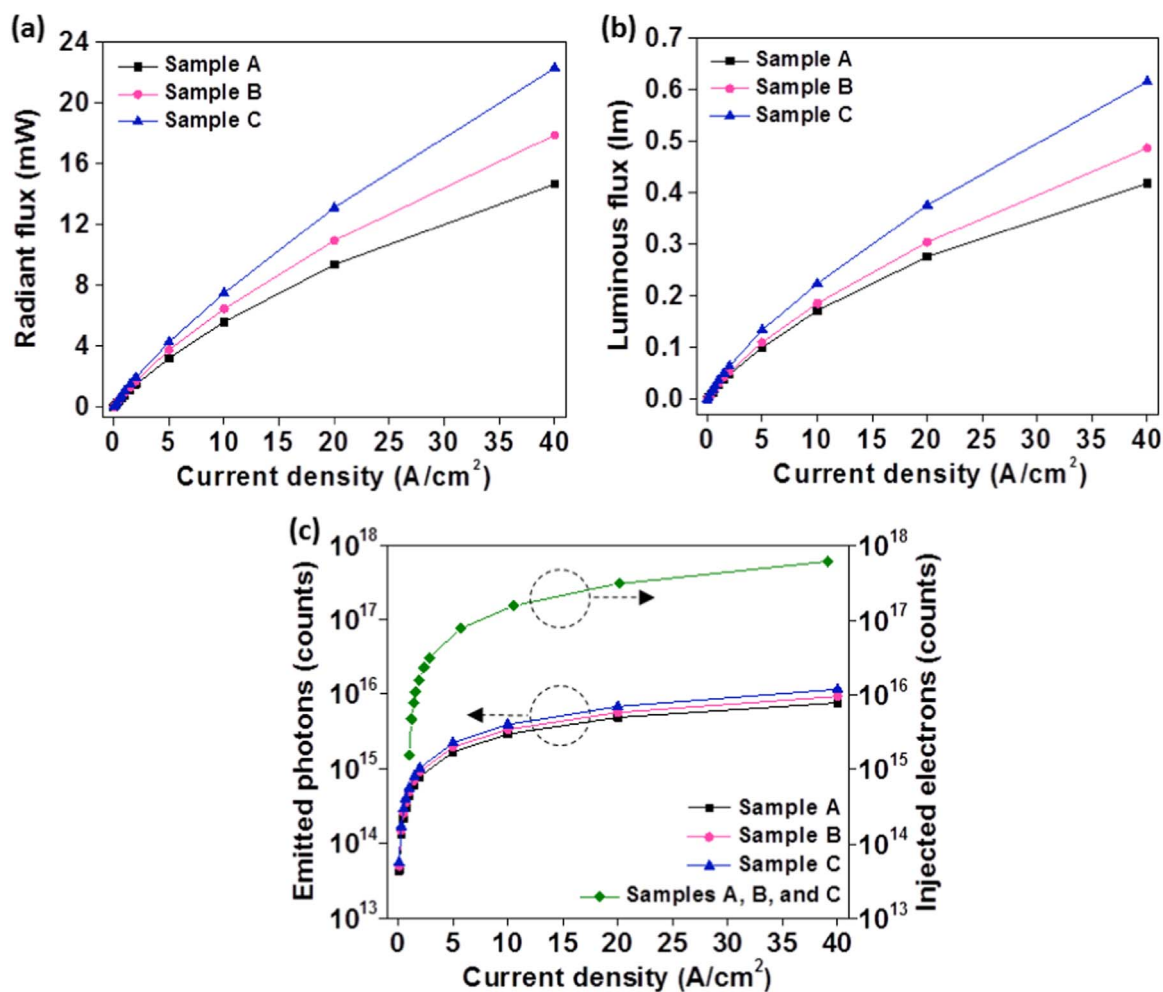


Fig. 6. Light output power of the LEDs. Plots of (a) Radiant flux and (b) luminous flux of the LEDs as a function of current density. (c) Plot of the number of emitted photons and injected electrons of the LEDs as a function of current density.

specific contact resistivity ( $\rho_c$ ) of the anode electrodes were measured by the circular transmission line method (CTLM) (Fig. S3). In addition, the epi-wafer was etched down for the cathode mesa and isolation process with consideration for the current spreading length and current crowding effect on the top surface (Fig. 3d–f). The vertical structure and electrodes dimension of the AlN/Al<sub>2</sub>O<sub>3</sub>-GaN LEDs are represented in Fig. 4a–b, in which the electrodes design of LEDs with consideration for the current spreading length was demonstrated by the light emission image with no current crowding effect. In addition, the calculated energy band diagram of the AlN/Al<sub>2</sub>O<sub>3</sub>-GaN LEDs with the increased surface potential, shown in Fig. 4c, supports the improved hole injection and light-emission efficiency thereafter.

### 3.4. Electrical characteristics of LEDs

The three samples characterized by XPS were fabricated together into LEDs. The vertical structure of the fabricated GaN LED with AlN/Al<sub>2</sub>O<sub>3</sub> stacked layers (sample C LED) and an optical image of the top view of the LED are shown in the inset of Fig. 5a. The LED has three anode fingers and two cathode fingers to maximize current spreading length and light-emission intensity. The equivalent circuit of the LED is shown in Fig. 5b.  $R_{AC}$  and  $R_{CC}$  are the anode and cathode contact resistances, respectively.  $R_B$  is the bulk series resistance and  $D_B$  represents the bulk diode. The surface states relating to leakage path in parallel with bulk current ( $I_B$ ) is labelled as  $I_S$ . It is noted that  $R_B$  is mainly due to the resistance of GaN:Mg. The surface leakage  $I_S$  can be reduced by the deposition of top surface layers [46]. The total current ( $I_{Total}$ ) consists of

$I_B$  and  $I_S$  and only  $I_B$  contributes to the radiative recombination for the LEDs. Fig. 3c shows the measured current density versus bias voltage of the three LEDs, in which the decreased current density level of sample B, 34.30 A/cm<sup>2</sup> at 5 V, is due to the reduced  $I_S$  with Al<sub>2</sub>O<sub>3</sub> passivation. And the current density levels of samples A and C, 36.95 A/cm<sup>2</sup> and 37.22 A/cm<sup>2</sup> at 5 V, respectively, are compared, in which the levels ( $I_{Total}$ ) of both samples look similar, but the  $I_{Total}$  of sample C consists of a reduced  $I_S$  by passivation and an increased  $I_B$  by the hole injection as compared to the current composition of sample A. Thus, a higher radiative recombination rate of sample C is expected. The diode ideality factors ( $n$ ) of the three types of LEDs were calculated to be 2.03 (sample A), 1.69 (sample B) and 1.58 (sample C) by the equation  $n = e/kT \cdot \delta V / \delta \ln I$ , where  $k$  is the Boltzmann constant [47]. The inset of Fig. 3c showed the decreased leakage current levels of sample B and C LEDs, which confirms the passivation effects of Al<sub>2</sub>O<sub>3</sub> and AlN/Al<sub>2</sub>O<sub>3</sub> at different levels, respectively.

The EL spectra of the three types of LEDs at driving current densities of 0.1, 0.3, 0.5, 0.7, 1, 1.5, 2, 5, 10, 20, and 40 A/cm<sup>2</sup> are exhibited in Fig. 5d–f, respectively. The insets in Fig. 5d–f show the EL spectra obtained at low current densities of 0.1, 0.3, 0.5, 1, 1.5, and 2 A/cm<sup>2</sup> (Fig. S4). The chromaticity coordinates of the EL spectra of the three LEDs are plotted within the adjacent blue area of the CIE 1931 chromaticity diagram in Fig. 5g. The optical light emission image of the sample C LED captured at 10 A/cm<sup>2</sup> is displayed in the inset of Fig. 5g. As can be seen in Fig. 5h, the EL intensity of sample B and C LEDs are higher than that of sample A LED, and the intensity of sample C LED is the highest at every driving current density levels. The highest EL peak intensity of

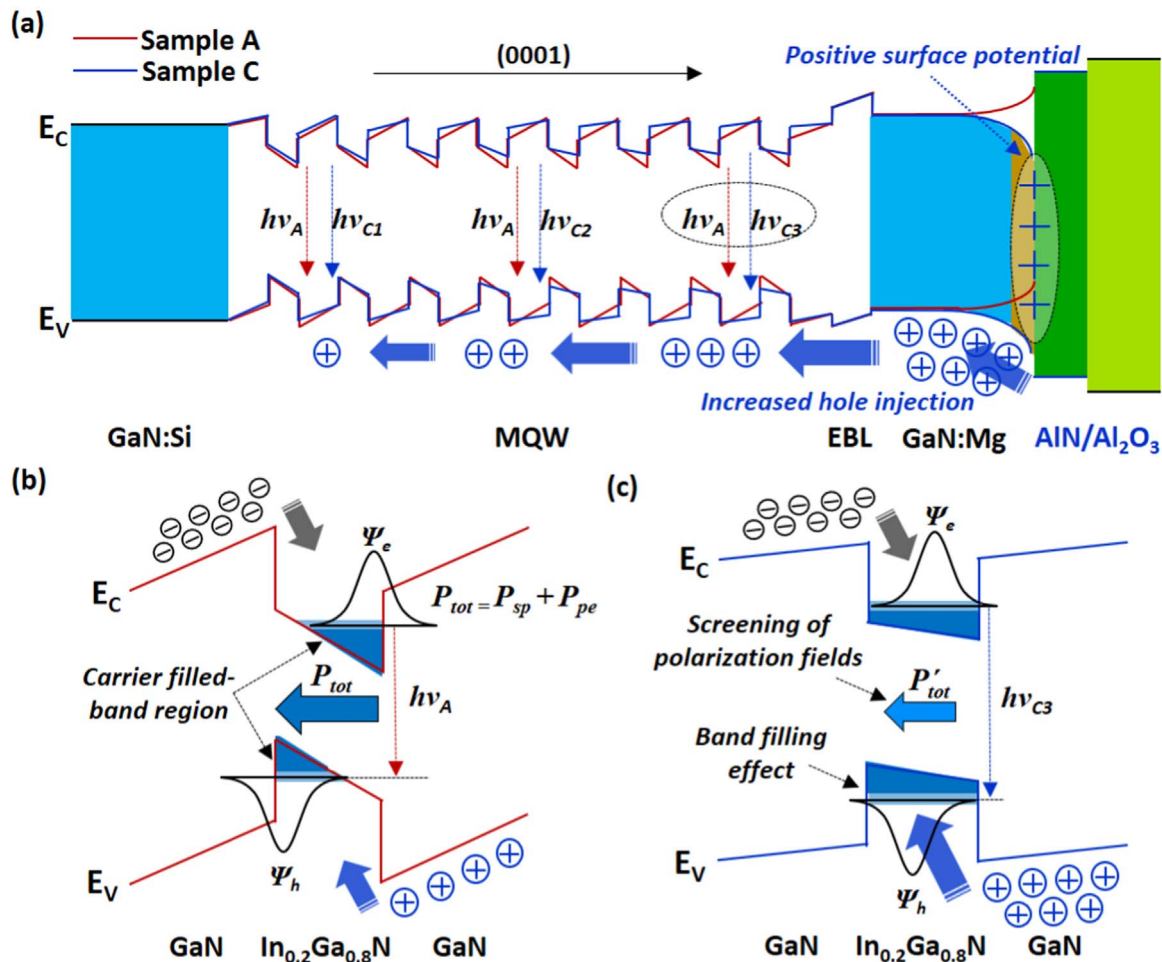


**Fig. 7.** Mechanism of LED performance enhancement. (a) Energy band diagrams of samples A and C.  $h\nu_A$  and  $h\nu_C$  represent the photon energies of samples A and C, respectively.  $h$  is Planck's constant and  $\nu$  is the frequency of the emitted light.  $h\nu_{C3} > h\nu_{C2} > h\nu_{C1}$ . Band diagrams of a single QW nearby GaN:Mg of (b) sample A and (c) sample C.  $\Psi_e$  and  $\Psi_h$  denote the electron and hole wave functions profiles in the QW. The total internal polarization fields ( $P_{total}$ ) composed of spontaneous polarization ( $P_{sp}$ ) and piezo-electric polarization fields ( $P_{pe}$ ) in the Wurtzite GaN LED (0001) tilt the slope of the QW and the wave functions separate, leading to a reduced radiative recombination rate and photon energy (i.e., quantum-confined Stark effect (QCSE)). The screened total polarization fields ( $P'_{tot}$ ) with the increased hole concentration in the QW result in a decreased slope of QW and an increased area of overlap in the wave functions, in addition to the band-filling effect. The above changes result in an increased radiative recombination rate and photon energy (i.e., suppression of QCSE).

sample C LED, compared to the other two samples, is ascribed to the increased electron-hole pair (EHP) recombination rate in the MQW due to the passivation and enhanced hole injection rate with the deposition of AlN/Al<sub>2</sub>O<sub>3</sub> stacked layers.

Interestingly, the EL peak wavelengths showed a blue-shift ( $\Delta\lambda$ ) as the driving current density increases (Fig. 5d-f). The EL peak wavelengths of the three types of LEDs as a function of driving current density are plotted in Fig. 5i. The blue shift is attributed to the band-filling of localized potential energy states and to the screening of internal polarization fields in the MQW by the injected carriers [28,48]. Specifically, the peak wavelengths of the LEDs at the current density of 0.1 A/cm<sup>2</sup> were 450.4 nm, 449.1 nm and 448.8 nm for samples A, B, and C LEDs, respectively. The peak wavelengths of the three samples were shifted to 445.4 nm (−5 nm), 444.9 nm (−4.2 nm), and 444.7 nm (−4.1 nm) as the current density increased to 40 A/cm<sup>2</sup>, respectively. The smallest blue-shift of peak wavelength ( $\Delta\lambda_c$ ) and the highest photon energy ( $E_{ph} = hc/\lambda$ , where  $h$  is the Planck's constant,  $c$  is the light velocity, and  $\lambda$  is the wavelength of light) of sample C LED indicate that the band-filling and screening of internal polarization effects were maximized by the deposition of AlN/Al<sub>2</sub>O<sub>3</sub> stacked layers in sample C.

Fig. 6a shows the plotted radiant flux of the three types of LEDs as a function of current density. The optical output power of sample B and C LEDs was improved by 22% and 52%, respectively, as compared to that

of the reference sample A LED at a current density of 40 A/cm<sup>2</sup>. The luminous flux as a function of current density shown in Fig. 6b also exhibits improved optical output power for sample B and C LEDs by 16% and 47%, respectively, as compared to that of sample A LED. The improved radiant flux and luminous flux of samples B and C LEDs are attributed to the passivation effects of Al<sub>2</sub>O<sub>3</sub> and AlN/Al<sub>2</sub>O<sub>3</sub> layers in addition to the increased hole injection rate by the AlN/Al<sub>2</sub>O<sub>3</sub> layers. The reduced surface recombination of holes with the AlN/Al<sub>2</sub>O<sub>3</sub> stacked layers also contributed to the improved output power. The reduced slopes of the radiant flux and luminous flux with increasing driving current density are probably due to the self-heating effect [48]. With the assumption that the initial radiative recombination coefficient inside the GaN LEDs is identical because of the identical epi-growth structures, the increased number of emitted photons from samples B and C LEDs is considered direct evidence supporting the effects of different top surface layers on the performance improvement of the LEDs.

Fig. 6c plotted the number of emitted photons and injected electrons for the LEDs, in which the number of emitted photons varies according to the sample types with the same number of injected electrons. Since the number of injected electrons is larger than the number of emitted photons, the increased photon emission of sample B and C LEDs is attributed to more hole injection into their MQW for the EHP recombination. In other words, the surface deposition layers enhanced the radiative recombination rate through surface passivation and the

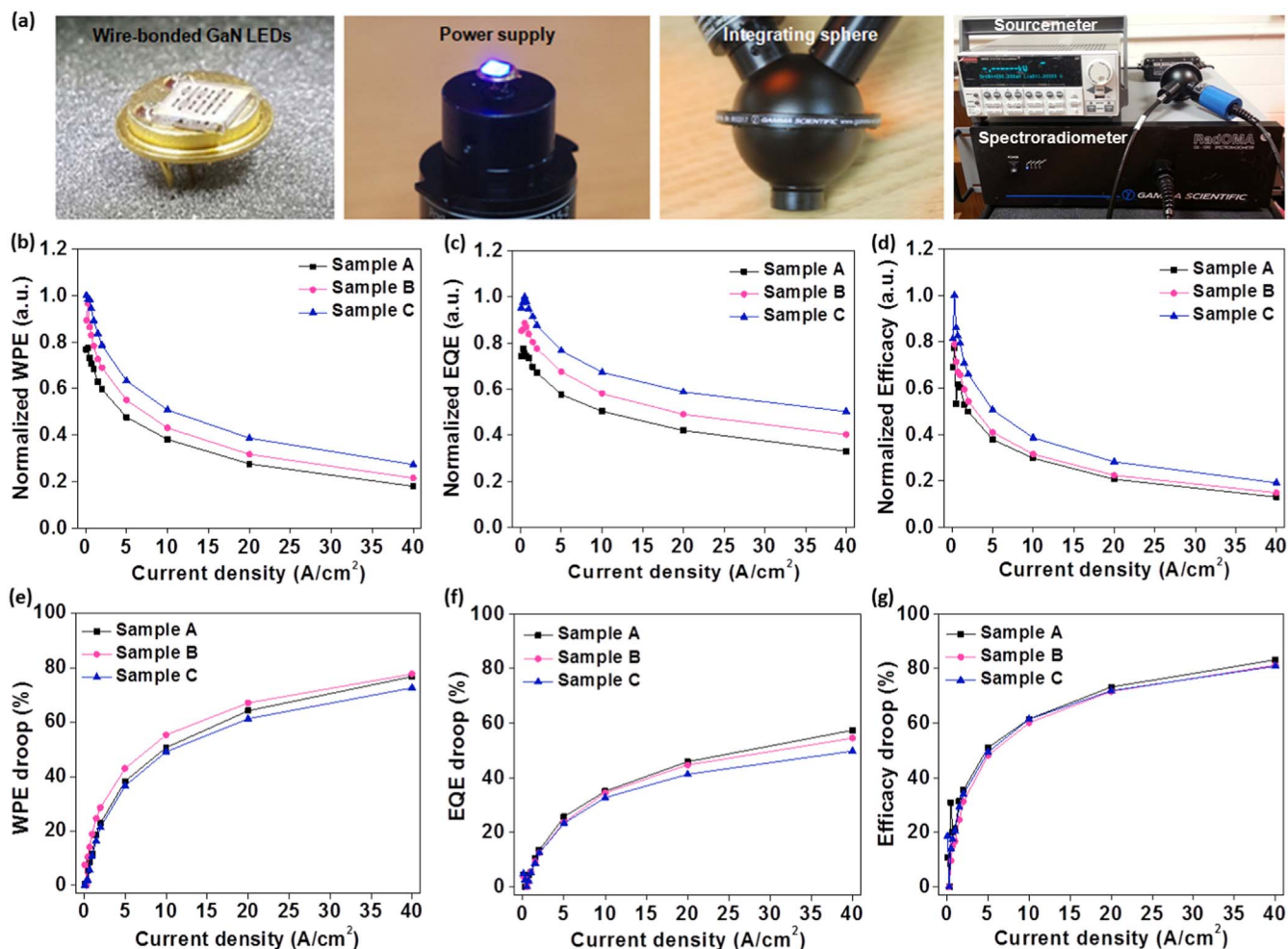


**Fig. 8.** Efficiency properties of LEDs. (a) Efficiency measurement setup: wire-bonding of the samples on sockets (all bare chips: no light extraction fixture was used), driving current bias with a power supply, light integration in a sphere, and efficiency analysis using a spectroradiometer. Normalized plots of (b) wall-plug efficiency (WPE), (f) external-quantum efficiency (EQE), and (g) efficacy as a function of current density. Efficiency droop rates of (e) WPE, (f) EQE, and (g) efficacy as a function of current density.

increase in hole injection.

### 3.5. Mechanism discussion

Fig. 7a depicts the energy band diagrams of samples A and C LEDs, in which the red and the blue solid lines represent the band diagrams before (sample A) and after (sample C) the deposition of AlN/Al<sub>2</sub>O<sub>3</sub> top surface layers. With the AlN/Al<sub>2</sub>O<sub>3</sub> layers, the positive surface potential was formed on the GaN at the AlN/GaN interface which induces the downward surface band bending and increases the hole injection rate into the MQW for radiative recombination. The increased number of injected holes induces the band-filling effect and the screening of internal polarization fields in the MQW of the GaN LED. Since the QWs in close proximity to the p-type GaN side benefits more from the increased hole injection than others far away, the band-filling and screening effects are more effective adjacent to the p-type side than the n-type side, thereby leading to enhanced photon energy in the MQW of sample C LED as  $h\nu_{C3} > h\nu_{C2} > h\nu_{C1}$ , where  $\nu$  is the frequency of the emitted light. Sample A LED, however, shows a similar photon energy ( $h\nu_A$ ) across the MQW. For a detailed explanation, the individual InGaN/GaN QWs of samples A and C LEDs next to the p-type GaN/EBL, enlarged in Fig. 7b and c, respectively, include injected charge carriers, electron and hole wave functions ( $\Psi_e$  and  $\Psi_h$ ), and total internal polarization fields ( $P_{tot}$ ) which consists of spontaneous polarization ( $P_{sp}$ ) and piezoelectric polarization ( $P_{pe}$ ) fields. In the QW of sample A LED (Fig. 7b), the internal polarization fields make the slope of the QW tilted, which

reduces spatial distribution of electron and hole wave functions. Due to the smaller overlapping area of wave functions, the EHP recombination rate becomes less efficient (i.e., QCSE). In the case of sample C LED with the increased hole injection rate into the QW (Fig. 7c), more holes injected into the QW occupy more energy bands (i.e., band filling effect) and compensate for the total internal polarization fields (i.e., screening effect). Therefore, the reduced polarization fields ( $P_{tot}$ ) decrease the energy slope of QW, leading to an increased overlap area and vertical distance between the electron and hole wave functions. As a result, the radiative recombination rate was improved and the energy of emitted photons is increased relative to sample A LED (i.e., suppression of QCSE). Specifically, the piezo-phototronic effect contributes to the increase in the radiative recombination rate by screening the piezoelectric field inside the QW with the increased hole concentration [49–62]. These effects altogether contribute to the enhanced radiative recombination rate and light emission efficiency of AlN/Al<sub>2</sub>O<sub>3</sub>-GaN LEDs.

### 3.6. LED efficiency characterizations

In order to assess the effects of the top surface layer deposition on the efficiency of LEDs, the wall-plug efficiency (WPE), external quantum efficiency (EQE), efficacy, and their droop rates were estimated for the three types LEDs. The setup for efficiency measurements is shown in Fig. 8a. The fabricated GaN LEDs first went through wire-bonding on sockets (all bare chips: no light extraction or thermal

management fixtures were used). Then the efficiency measurements were carried out using an integrating sphere. The normalized values of WPE, EQE, and efficacy as a function of current density for samples A, B, and C LEDs are shown in Fig. 8b–d (for measurement data, see Figs. S5–S7). The droop rates of WPE, EQE, and efficacy of the three types of LEDs as a function of current density are shown in Fig. 8e–g. From the comparisons, the sample C LED shows the highest performance among the three types. The peak WPE at 0.3 A/cm<sup>2</sup> and the droop rate at 40 A/cm<sup>2</sup> of sample C LED were improved by 29% and 13%, respectively, compared to the sample A LED. The peak EQE and efficacy values of sample C LED were improved by 29% and 30%, respectively, as compared to sample A LED. For the droop rates of EQE and efficacy, the sample C LED showed 6% and 3% improved droop rates at 40 A/cm<sup>2</sup>, respectively, as compared to sample A LED. The enhanced peak efficiencies and reduced droop rates of the sample C LED are ascribed to the improved radiative recombination rate and reduced electron leakage in the MQW with the increased hole injection [63]. The increased hole concentration in the MQW for sample C LED reduces the asymmetry of concentrations of electrons and therefore contributes to more recombination of EHPs.

#### 4. Conclusions

With the top surface deposition of AlN/Al<sub>2</sub>O<sub>3</sub> stacked layers, the peak efficiency values of WPE, EQE, and efficacy of the GaN LEDs were improved by 29%, 29% and 30%, respectively, and their corresponding efficiency droop rates were decreased by 13%, 6% and 3%, separately. The AlN/Al<sub>2</sub>O<sub>3</sub> layers reduced the surface defect states of p-GaN layer and enhanced hole injection rate into the MQW by increasing the surface potential of GaN. In addition, the increased hole injection into the MQW induced the band-filling effect and screened the internal polarization fields, and thus increased the symmetry of electron and hole concentrations in MQW. The improved radiative recombination rate and reduced electron leakage in the MQW enhanced the peak efficiency and efficiency droop rates of the GaN LEDs with top surface AlN/Al<sub>2</sub>O<sub>3</sub> layers.

#### Acknowledgements

This work was supported by Wisconsin Alumni Research Foundation's (WARF) Accelerator Program. The work was also partly supported by Office of Naval Research (ONR) under Grant N00014-13-1-0226 (PM: Dr. Paul Maki).

#### Author contributions

K. Kim, K. J. Chen and Z. Ma designed the experiments. K. Kim, D. Liu and Z. Ma conducted manuscript writing. M. Hua and K. J. Chen conducted ALD and characterizations. K. Kim and J. Kim conducted device fabrication. All authors contributed to data analysis and manuscript revisions. Z. Ma conceived the research.

#### Appendix A. Supporting information

Supplementary data associated with this article can be found in the online version at <http://dx.doi.org/10.1016/j.nanoen.2017.11.047>.

#### References

- [1] S. Nakamura, M. Senoh, T. Mukai, *Jpn. J. Appl. Phys.* 32 (1993) L8–L11.
- [2] J.H. Choi, A. Zoukarniev, S.I. Kim, C.W. Baik, M.H. Yang, S.S. Park, H. Suh, U.J. Kim, H.B. Son, J.S. Lee, M. Kim, J.M. Kim, K. Kim, *Nat. Photonics* 5 (2011) 763–769.
- [3] J.J. Wierer, A. David, M.M. Megens, *Nat. Photonics* 3 (2009) 163–169.
- [4] E. Matioli, S. Brinkley, K.M. Kelchner, Y. Hu, S. Nakamura, S. DenBaars, J. Speck, C. Weisbuch, *Light Sci. Appl.* 1 (2012) e22.
- [5] I.H. Lee, L.W. Jang, A.Y. Polyakov, *Nano Energy* 13 (2015) 140–173.
- [6] Z. Wu, Y. Lu, W. Xu, Y. Zhang, J. Li, S. Lin, *Nano Energy* 30 (2016) 362–367.
- [7] L. Wang, W. Liu, Y. Zhang, Z.H. Zhang, S.T. Tan, X. Yi, G. Wang, X. Sun, H. Zhu, H.V. Demir, *Nano Energy* 12 (2015) 419–436.
- [8] M.S. Kang, C.H. Lee, J.B. Park, H. Yoo, G.C. Yi, *Nano Energy* 1 (2012) 391–400.
- [9] T.R. Kuykendall, A.M. Schwartzberg, S. Aloni, *Adv. Mater.* 27 (2015) 5805–5812.
- [10] O. Lupan, T. Pauporte, B. Viana, *Adv. Mater.* 22 (2010) 3298–3302.
- [11] Y.J. Hong, C.H. Lee, A. Yoon, M. Kim, H.K. Seong, H.J. Chung, C. Sone, Y.J. Park, G.C. Yi, *Adv. Mater.* 23 (2011) 3284–3288.
- [12] K. Chung, H. Yoo, J.K. Hyun, H. Oh, Y. Tchoe, K. Lee, H. Baek, M. Kim, G.C. Yi, *Adv. Mater.* 28 (2016) 7688–7694.
- [13] C. Pan, M. Chen, R. Yu, Q. Yang, Y. Hu, Y. Zhang, Z.L. Wang, *Adv. Mater.* 28 (2016) 1535–1552.
- [14] S.F. Chichibu, K. Kojima, A. Uedono, Y. Sato, *Adv. Mater.* 29 (2017) 1603644.
- [15] S.C. Tsai, C.H. Lu, C.P. Liu, *Nano Energy* 28 (2016) 373–379.
- [16] H. Morkoc, S.N. Mohammad, *Science* 267 (1995) 51–55.
- [17] H. Jeong, S.Y. Jeong, D.J. Park, H.J. Jeong, S. Jeong, J.T. Han, H.J. Jeong, S. Yang, H.Y. Kim, K.J. Baeg, S.J. Park, Y.H. Ahn, E.K. Suh, G.W. Lee, Y.H. Lee, M.S. Jeong, *Sci. Rep.* 5 (2015) 7778.
- [18] F. Bernardini, V. Fiorentini, D. Vanderbilt, *Phys. Rev. B* 56 (1997) R10024–R10027.
- [19] S. Kim, S. Cho, J. Jeong, S. Kim, S. Hwang, G. Kim, S. Yoon, B.G. Park, *Opt. Express* 25 (2017) 6440–6449.
- [20] J. Kim, Y.H. Cho, D.S. Ko, X.S. Li, J.Y. Won, E. Lee, S.H. Park, J.Y. Kim, S. Kim, *Opt. Express* 22 (2014) A857–A866.
- [21] D.H. Hsieh, A.J. Tzou, T.S. Kao, F.I. Lai, D.W. Lin, B.C. Lin, T.C. Lu, W.C. Lai, C.H. Chen, H.C. Kuo, *Opt. Express* 23 (2010) 5466–5471.
- [22] C. Jia, T. Yu, H. Lu, C. Zhong, Y. Sun, Y. Tong, G. Zhang, *Opt. Express* 21 (2013) 8444–8449.
- [23] G. Kim, M.C. Sun, J.H. Kim, E. Park, B.G. Park, *Appl. Phys. Lett.* 110 (2017) 021115.
- [24] Y.H. Kuo, Y.K. Lee, Y. Ge, S. Ren, J.E. Roth, T.I. Kamins, D.A.B. Miller, J.S. Harris, *Nature* 437 (2005) 1334–1336.
- [25] P. Waltereit, O. Brandt, A. Trampert, H.T. Grahn, J. Menniger, M. Ramsteiner, M. Reiche, K.H. Ploog, *Nature* 406 (2000) 865–868.
- [26] T. Deguchi, K. Sekiguchi, A. Nakamura, T. Sota, R. Matsuo, S. Chichibu, S. Nakamura, *Jpn. J. Appl. Phys.* 38 (1999) L914–L916.
- [27] D.A.B. Miller, D.S. Chemla, T.C. Damen, A.C. Gossard, W. Wiegmann, T.H. Wood, C.A. Burrus, *Phys. Rev. Lett.* 53 (1984) 2173–2176.
- [28] C.Y. Cho, S.J. Park, *Opt. Express* 24 (2016) 7488–7494.
- [29] V.C. Su, P.H. Chen, R.M. Lin, M.L. Lee, Y.H. You, C.I. Ho, Y.C. Chen, W.F. Chen, C.H. Kuan, *Opt. Express* 21 (2013) 30065–30073.
- [30] J.H. Ryou, W. Lee, J. Limb, D. You, J.P. Liu, R.D. Dupuis, Z.H. Wu, A.M. Fischer, F.A. Ponce, *Appl. Phys. Lett.* 92 (2008) 101113.
- [31] B. Janjua, H. Sun, C. Zhao, D.H. Anjum, D. Priante, A.A. Alhamoud, F. Wu, X. Li, A.M. Albadi, A.Y. Alyamani, M.M. Eldesouki, T.K. Ng, B.S. Ooi, *Opt. Express* 25 (2017) 1381–1390.
- [32] A.A. Toropov, E.A. Shevchenko, T.V. Shubina, V.N. Jmerik, D.V. Nechaev, M.A. Yagovkina, A.A. Sitnikova, S.V. Ivanov, G. Pozina, J.P. Bergman, B. Monemar, *J. Appl. Phys.* 114 (2013) 124306.
- [33] Z.H. Zhang, W. Liu, Z. Ju, S.T. Tan, Y. Ji, Z. Kyaw, X. Zhang, L. Wang, X.W. Sun, H.V. Demir, *Appl. Phys. Lett.* 104 (2014) 243501.
- [34] H.S. Chen, D.M. Yeh, Y.C. Lu, C.Y. Chen, C.F. Huang, T.Y. Tang, C.C. Yang, C.S. Wu, C.D. Chen, *Nanotechnology* 17 (2006) 1454–1458.
- [35] K. Okamoto, I. Niki, A. Scherer, Y. Narukawa, T. Mukai, Y. Kawakami, *Appl. Phys. Lett.* 87 (2005) 071102.
- [36] S. Huang, Q. Jiang, S. Yang, C. Zhou, K.J. Chen, *IEEE Electron Device Lett.* 33 (2012) 516–518.
- [37] H. Wang, C. Liu, Q. Jiang, Z. Tang, K.J. Chen, *IEEE Electron Device Lett.* 36 (2015) 760–762.
- [38] S. Liu, S. Yang, Z. Tang, Q. Jiang, C. Liu, M. Wang, K.J. Chen, *IEEE Electron Device Lett.* 35 (2014) 723–725.
- [39] S. Huang, Q. Jiang, S. Yang, Z. Tang, K.J. Chen, *IEEE Electron Device Lett.* 34 (2013) 193–195.
- [40] C. Liu, S. Liu, S. Huang, K.J. Chen, *IEEE Electron Device Lett.* 34 (2013) 1106–1108.
- [41] S. Liu, S. Yang, Z. Tang, Q. Jiang, C. Liu, M. Wang, B. Shen, K.J. Chen, *Appl. Phys. Lett.* 106 (2015) 051605.
- [42] K.C. Mishra, P.C. Schmidt, S. Laubach, K.H. Johnson, *Phys. Rev. B* 76 (2007) 035127.
- [43] D.M. Zhermoleto, M.A. Negara, R.D. Long, S. Aloni, D. Nordlund, P.C. McIntyre, *ACS Appl. Mater. Interfaces* 7 (2015) 12774–12780.
- [44] K.S.A. Butcher, H. Timmers, Afifuddin, P.P.T. Chen, T.D.M. Weijers, E.M. Goldys, T.L. Tansley, R.G. Elliman, J.A. Freitas Jr., *J. Appl. Phys.* 92 (2002) 3397–3403.
- [45] J. Yang, B.S. Eller, C. Zhu, C. England, R.J. Nemanich, *J. Appl. Phys.* 112 (2012) 053710.
- [46] C.M. Yang, D.S. Kim, Y.S. Park, J.H. Lee, Y.S. Lee, J.H. Lee, *Opt. Photonics J.* 2 (2012) 185–192.
- [47] K. Kim, Y. Jeon, K. Cho, S. Kim, *ACS Appl. Mater. Interfaces* 8 (2016) 2764–2773.
- [48] F. Akyol, D.N. Nath, E. Gür, P.S. Park, S. Rajan, *Jpn. J. Appl. Phys.* 50 (2011) 052101.
- [49] W. Wu, Z.L. Wang, *Nat. Rev. Mater.* 1 (2016) 1–17.
- [50] W. Wu, L. Wang, R. Yu, Y. Liu, S.H. Wei, J. Hone, Z.L. Wang, *Adv. Mater.* 28 (2016) 8463–8468.
- [51] W. Wu, *NPS Asia Mater.* 8 (2016) e267.
- [52] F. Xue, L. Yang, M. Chen, J. Chen, X. Yang, L. Wang, L. Chen, C. Pan, Z.L. Wang, *NPG Asia Mater.* 9 (2017) e418.
- [53] C. Jiang, L. Jing, X. Huang, M. Liu, C. Du, T. Liu, X. Pu, W. Hu, Z.L. Wang, *ACS Nano* 11 (2017) 9405–9412.
- [54] X. Wang, R. Yu, C. Jiang, W. Hu, W. Wu, Y. Ding, W. Peng, S. Li, Z.L. Wang, *Adv.*

- Mater. 28 (2016) 7234–7242.
- [55] X. Huang, C. Du, Y. Zhou, C. Jiang, X. Pu, W. Liu, W. Hu, H. Chen, Z.L. Wang, ACS Nano 10 (2016) 5145–5152.
- [56] X. Huang, C. Jiang, C. Du, L. Jing, M. Liu, W. Hu, Z.L. Wang, ACS Nano 10 (2016) 11420–11427.
- [57] S.C. Tsai, C.H. Lu, C.P. Liu, Nano Energy 28 (2016) 373–379.
- [58] C.Y. Tsai, K. Gupta, C.H. Wang, C.P. Liu, Nano Energy 34 (2017) 367–374.
- [59] W. Song, X. Wang, C. Xia, R. Wang, L. Zhao, D. Guo, H. Chen, J. Xiao, S. Su, S. Li, Nano Energy 33 (2017) 272–279.
- [60] X.X. Yu, H. Yin, H.X. Li, W. Zhang, H. Zhao, C. Li, M.Q. Zhu, Nano Energy 34 (2017) 155–163.
- [61] W. Wu, C. Pan, Y. Zhang, X. Wen, Z.L. Wang, Nano Today 8 (2013) 619–642.
- [62] Z.L. Wang, Adv. Mater. 24 (2012) 4632–4646.
- [63] J. Cho, E.F. Schubert, J.K. Kim, Laser Photonics Rev. 7 (2013) 408–421.



**Kwangeun Kim** received the B.S. and M.S. degrees in Electrical Engineering from Korea University, Seoul, Korea in 2009 and 2011, respectively, and M.S. degree in Electrical and Computer Engineering from the University of Wisconsin-Madison, Madison, WI, USA, in 2015, where he is currently pursuing the Ph.D. degree. Since 2013, he has been a Research Assistant with the University of Wisconsin-Madison. Between 2011 and 2013, he worked for Korean Standards Association, Seoul, Korea.



**Dr. Mengyuan Hua** received the B.S. degree in Physics from Tsinghua University, Beijing, China, in 2013. She then joined the Hong Kong University of Science and Technology (HKUST), Hong Kong, China, where she received the Ph.D. degree in Electronic and Computer Engineering in 2017 under the supervision of Prof. Kevin J. Chen. Currently, she is a research associate at HKUST. Her research interests include GaN-based power device technology and device reliability.



**Dr. Dong Liu** received her Ph.D degree in Electrical Engineering Department of Tsinghua University, Beijing, China. She is currently a Research Associate in the Department of Electrical and Computer Engineering at the University of Wisconsin-Madison. Her research interests include optoelectronics, flexible optoelectronics, and nanophotonics.



**Jisoo Kim** received the B.S. from Ajou University, Suwon, Korea and M.E. degrees from Korea University, Seoul, Korea, in 2011. Since September 2015, he is studying for a Ph.D. in electrical and computer engineering in University of Wisconsin-Madison. His research interests include heterojunction semiconductor device with 2port and three port device such as solar cell, LED, and HBT by nanomembrane transfer. Between 2011 and 2014, Jisoo worked as junior researcher in Shinsung solar energy Co. Ltd., Korea, conducting to improve efficiency of silicon solar cell.



**Prof. Kevin J. Chen** received his B.S. degree from Peking University, Beijing, China in 1988, and Ph.D. degree from University of Maryland, College Park, USA in 1993. His industry experience includes carrying out research and development on III-V high-speed devices in NTT LSI Laboratories, Atsugi, Japan and Agilent Technologies Inc., Santa Clara, California, USA. Prof. Chen joined Hong Kong University of Science and Technology (HKUST) in 2000, where he is currently a professor in the Department of Electronic and Computer Engineering. At HKUST, he has carried out research in wide-bandgap III-nitride devices and ICs, GaN-based MEMS devices, silicon-based microwave passive components and 3D through-silicon via interconnects, and multi-band reconfigurable microwave filters. Currently, his group is focused on developing GaN device technologies for power electronics and high-temperature electronics applications. Prof. Chen has authored or co-authored more than 280 publications in international journals and conference proceedings. He has been granted 4 US patents.



**Prof. Zhenqiang (Jack) Ma** received dual Bachelor's degrees in Applied Physics and Electrical Engineering from Tsinghua University, Beijing, China, and a Ph.D. degree in Electrical Engineering from the University of Michigan–Ann Arbor. He is currently a Lynn H. Matthias Professor in Engineering and Vilas Distinguished Achievement Professor in the Department of Electrical and Computer Engineering at the University of Wisconsin–Madison. Prof. Ma has a broad range of research interests including lattice-mismatched semiconductor heterostructures, high-speed RF devices, power electronics, flexible/stretchable electronics and optoelectronics, and bioelectronics.